

# Time-gated optical system for depth-resolved functional brain imaging

Juliette Selb

Danny K. Joseph

David A. Boas

Massachusetts General Hospital  
Athinoula A. Martinos Center  
Photon Migration Imaging Laboratory  
Building 149, 13th Street  
Charlestown, Massachusetts 02129  
E-mail: juliette@nmr.mgh.harvard.edu

**Abstract.** We present a time-domain optical system for functional imaging of the adult head. We first describe the instrument, which is based on a Ti:Sapphire pulsed laser (wavelength 750–850 nm) and an intensified CCD camera enabling parallel detection of multiple fibers. We characterize the system in terms of sensitivity and signal-to-noise ratio, instrument response function, cross-talk, stability, and reproducibility. We then describe two applications of the instrument: the characterization of baseline optical properties of homogeneous scattering media, and functional brain imaging. For the second application, we developed a two-part probe consisting in two squares of  $4 \times 4$  sources and  $3 \times 3$  detectors. The laser source is time-multiplexed to define 4 states of 8 sources that can be turned on during the same camera frame while minimizing cross-talk. On the detection side, we use for each detector 7 fibers of different lengths creating an optical delay, and enabling simultaneous detection in 7 windows (by steps of 500 ps) for each detector. This multiple window detection allows depth sensitivity. The imaging probe was tested on dynamic phantoms and a preliminary result on an adult performing a motor task shows discrimination between superficial and cortical responses to the stimulus on both hemispheres. © 2006 Society of Photo-Optical Instrumentation Engineers. [DOI: 10.1117/1.2337320]

Keywords: diffuse optical tomography; time domain system; optical properties characterization; depth-resolved imaging; functional brain imaging.

Paper 05368R received Dec. 6, 2005; revised manuscript received Apr. 10, 2006; accepted for publication Apr. 26, 2006; published online Aug. 31, 2006.

## 1 Introduction

Diffuse optical imaging (DOI) has developed over the past 15 years as a method for functional brain imaging.<sup>1–5</sup> By measuring optical absorption changes in the near-infrared spectrum, DOI assesses oxy-hemoglobin (HbO) and deoxy-hemoglobin (HbR) concentration changes and can monitor hemodynamic signals related to cerebral activation. By using multiple source and detector fiber positions on the head, regional mapping of cerebral blood volume and oxygen saturation can be achieved with a resolution of a couple centimeters in humans.<sup>6</sup> In the field of functional imaging, DOI has caused a growing interest because of the new contrasts it yields (simultaneous HbO and HbR), combined with advantages of portability, low cost, low sensitivity to movements, and high temporal resolution. Functional neuroimaging applications with diffuse light have included studies of motor,<sup>6,7</sup> somatosensory,<sup>6</sup> visual,<sup>8,9</sup> auditory,<sup>10</sup> cognitive,<sup>2</sup> and language<sup>11</sup> stimuli. The main drawbacks of the method remain its poor spatial resolution and limited depth sensitivity due to the strong scattering of light by biological tissues. The sensitivity of a single source–detector pair measurement covers a large tissue volume and includes contributions from both superficial and cerebral tis-

ues. Continuous-wave (CW) systems, which are the simplest and most commonly used systems in this field, generally give measurements of brain activation impeded by superficial systemic signals.<sup>12</sup>

Solutions to overcome superficial signals have included principal component analysis to filter systemic contributions from brain activation,<sup>12,13</sup> multidistance CW measurements to probe different depths,<sup>14</sup> and frequency-domain (FD) measurements where amplitude and phase have different depth sensitivity.<sup>15</sup> In 2001, Steinbrink et al. showed theoretically and experimentally that single-distance time-domain (TD) measurements could discriminate between superficial and cerebral absorption changes by making use of photon time of flight distributions.<sup>16</sup> They distinguished between extra- and intra-cerebral signals during a Valsalva maneuver, and a functional activation of the motor cortex. Using three moments of the distribution of the times of flights (DTOF) of photons at multiple distances, Liebert et al. performed depth discrimination during an ICG bolus injection.<sup>17</sup> Recently, we presented depth-resolved measurements acquired with a time-gated TD system to distinguish superficial systemic signals and cerebral activation during a finger-tapping task.<sup>18</sup> We also demonstrated theoretically the improvement of TD over CW in terms of depth sensitivity. Montcel et al. published similar results with a single-photon counting system.<sup>19</sup>

Address all correspondence to Juliette Selb, Photon Migration Imaging Laboratory, Massachusetts General Hospital, Athinoula A. Martinos Center – Building 149, 13th Street, Charlestown, MA 02129; Tel: 617–726–9338; Fax: 617–726–7422; E-mail: juliette@nmr.mgh.harvard.edu

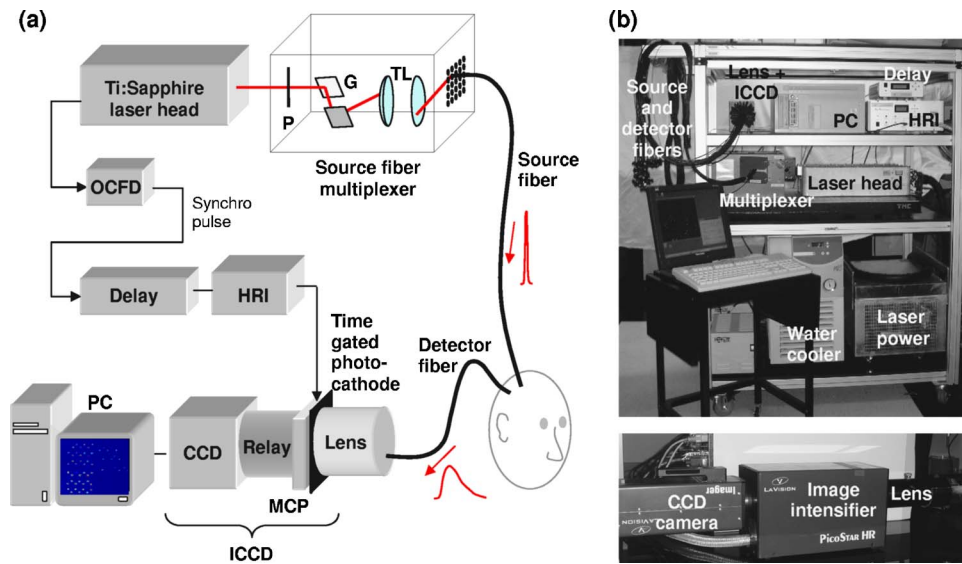


**Fig. 1** Time-domain instrument scheme (a) and picture (b). *P*: Polarizer; *G*: Galvanometer mirrors; *TL*: telecentric lens; *OCFD*: Optical constant fraction discriminator; *HRI*: high rate imager; *CCD*: charge coupled device camera; *MCP*: MicroChannel plate.

So far, these TD studies showing depth resolution were performed with a small probe set over a localized region of interest on the head (above the motor cortex in most cases), and yielding local measurements. Current work in the domain of time domain DOI is advancing toward imaging of the human cortex. Different teams are developing TD imaging systems characterized on phantoms.<sup>20–23</sup> Wabnitz et al. have presented the first data showing 1 Hz functional imaging ( $3 \times 3$  sources,  $2 \times 2$  detectors) with depth sensitivity on an adult head during a finger-tapping task.<sup>21</sup> One major difficulty to address is the acquisition frequency of such systems: for functional imaging, an image rate better than 1 Hz is desirable. This is particularly challenging when longer integration times are required for the weaker signals of the later arriving photons, which carry information from a greater depth.

These previous works motivated the development of a TD system providing both a large number of sources and detectors and a higher temporal resolution. In this paper, we present the time-gated single-wavelength system, which we propose to use for depth-resolved functional imaging of both hemispheres of the adult human head. This system is capable of 1.8 Hz acquisition. The instrument is based on a Ti:Sapphire pulsed laser and the parallel gated detection of multiple fibers on an intensified CCD camera. We first describe the general design and technical conception of the instrument. We then detail its characterization in terms of sensitivity, signal-to-noise ratio, instrument response function, cross-talk, stability, and reproducibility. The third and fourth parts present two different applications of the system, respectively, the determination of absolute optical properties of turbid media, and functional imaging. Finally, we show results on dynamic phantoms and preliminary data on a volunteer subject during motor stimulation.

## 2 System Description

In a time domain setup, a short pulse of light (typically 1–100 ps) is injected into the studied scattering medium, and,

after propagation through the medium, the broadened and attenuated pulse is measured by a fast time-resolved detector. Two elements of a time domain system are therefore essential: a pulsed source and a time-resolved detector. Our time-domain imager is schematically represented on Fig. 1(a), with the picture of the actual system shown in Fig. 1(b).

### 2.1 Source

The system uses a pulsed Titanium:Sapphire laser (Mai Tai, Spectra Physics) with a 80 MHz repetition rate, emitting in the near infrared with a tunable wavelength between 750 and 850 nm and a spectral bandwidth of  $\sim 10$  nm. The emitted pulses are approximately 100 fs wide. The maximum average exit power is 1 W, which can be attenuated by a rotating polarizer. The laser beam enters a multiplexer, which redirects the beam in two dimensions with two mirrors driven by a software-controlled bi-axial galvanometer. In this way, the laser beam is directed into one of an array of fibers (42 fibers in the present configuration) through a telecentric focusing lens.

The pulsed laser we use offers the advantages of wavelength tunability over 100 nm, and high output power enabling time-multiplexing of the source over multiple positions. On the other hand, it has the main drawback of being limited to a single wavelength. It is thus not possible to extract concentrations of oxy- and deoxy-hemoglobin from our measurements, as dual- (or multiple-) wavelength systems provide. At 830 nm, the changes in intensity that we detect result from a combination of changes in blood volume and oxygenation. By working at 800 nm, we can monitor changes in local blood volume, but we lack the information on oxygen saturation changes. In the future, we expect the technological development of laser sources to enable us more flexibility. For instance, the source could be updated to a dual-wavelength pulsed fiber laser, as in the MONSTIR system used by Hebdén et al.<sup>22</sup>

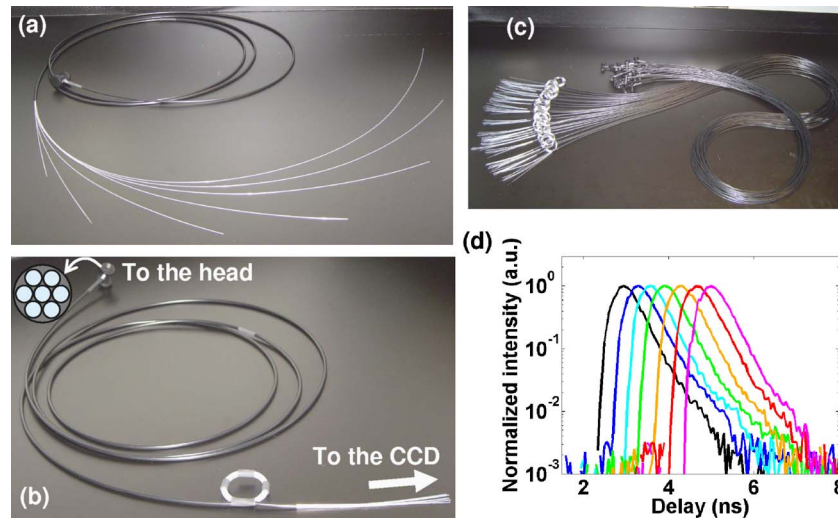


**Fig. 2** Detector fibers. (a) Seven fibers of different lengths for one detector position. (b) The same 7 fibers after being looped together. The small scheme shows the 7 fiber geometry on the head side. (c) The 25 detector bundles. (d) TPSF recorded on a scattering phantom by the 7 fibers of a same detector bundle.

## 2.2 Detector

While most existing time-domain systems are based on a time-correlated single-photon counting (TCSPC) detection,<sup>16,17,19–21,23–26</sup> the use of time-gated detectors has also been reported by a few teams for early photon detection or diffuse optical tomography.<sup>18,27–29</sup> Our system performs a gated detection of the temporal point spread function (TPSF) through narrow temporal windows. The detector is an Intensified Charge Coupled Device (ICCD) camera (*PicoStar HR, LaVision*), which comprises an image intensifier followed by a 12-bit CCD camera of 1370 by 1040 pixels. The ICCD acts as a very fast shutter synchronized with the laser pulses through a delay unit (*PS-Delay Unit, LaVision*). The delay between the laser pulses and their gated detection can be adjusted with a 25-ps step. The gate width is adjustable by steps of 100 ps from 300 ps to 1000 ps. After the image intensifier, the CCD camera integrates light over a typical exposure time of 100 ms, i.e., 8 million successive laser pulses. Because of the transfer time to the PC, the actual CCD acquisition frame is a bit lower than 8 Hz for this exposure time.

We use 3-meter-long, step-index, multimode, silica optical fibers (core diameter 400  $\mu\text{m}$ , NA 0.39, *Tecs, Thorlabs*) to bring light from the laser multiplexer to the studied medium and from the medium to the ICCD (core diameter 300  $\mu\text{m}$  and 400  $\mu\text{m}$ ). An objective lens of unit magnification images the tips of the fibers onto the photocathode of the ICCD. In the present configuration, we have a total of 175 fibers imaged in parallel onto the CCD.

## 2.3 TPSF Measurement

The temporal point spread functions (TPSF) are measured through the temporal gate provided by the image intensifier. To record the whole TPSF, this gate is electronically scanned, providing a measure of the true TPSF convolved by the instrument response function, whose width is a combination of the gate width and the dispersion in the fibers. However, this electronic delay scanning is too slow for functional imaging,

where we desire acquisition frequencies higher than 1 Hz. The time to change the delay is 370 ms, which leads to measurement times from a few seconds up to a couple of minutes depending on the number of measurement points of the TPSF we choose to record. Alternatively to the electronic delay, we implemented “hardware” optical delays enabling simultaneous measurements in various temporal gates. For each detector position, we use 7 fibers of different lengths, which introduce different delays to the measurement (see pictures of the fibers on Figs. 2(a)–2(c)). With 10-cm increments in each fiber length, we create 500-ps delays between fibers. On the head, the 7 fibers at each position are arranged in a hexagonal pattern (Fig. 2(b)) and cover an area of about 2-mm diameter. These 7 individual fibers are then resolved by the CCD such that the different time delays are simultaneously imaged.

We therefore have two modes of operation of our instrument. The first mode is the electronic scan of the delay, which provides a slow (up to 2 minutes) but finely resolved (down to 25-ps steps) measure of a TPSF. This is the mode we use for characterizing the static optical properties of a medium. In that mode, the 7 fibers at each position measure the same signal, simply delayed from one fiber to another (see Fig. 2(d)). Although they do not offer extra information, they can be used to increase the signal-to-noise ratio. The second operation mode is a continuous grabbing of CCD frames at a fixed temporal delay. In that mode, the 7 fibers at each position enable us to achieve parallel acquisition in 7 different time gates. We record the evolution of the TPSF at all sampling delays simultaneously. Since it has better temporal resolution, this mode is used for functional imaging.

## 3 System Characterization

We characterized the performance of our system in terms of signal-to-noise ratio (SNR), stability, reproducibility, and cross-talk.



### 3.1 Warm-up Time

All parts of the equipment require time to reach steady-state thermal equilibrium. After initial warm-up, both the ICCD and the multiplexer stay within 0.2% of their asymptotic value within a 30-minute period. The laser requires about an hour to reach the same level. It also requires approximately 30 minutes of pre-warm-up before turning the pump diodes on. The characterizations presented ahead were performed after all elements of the time domain system were turned on for at least 1.5 hours to avoid any system drift associated with warm-up.

### 3.2 ICCD Sensitivity and Signal-to-Noise Ratio

In this part, we summarize the theoretical description of the signal-to-noise ratio (SNR) of an ICCD presented by Brukilacchio in his Ph.D. thesis,<sup>30</sup> and we present our own experimental SNR characterization of our system.

We first briefly summarize the principle of operation of the ICCD. The image intensifier consists of a photocathode, a microchannel plate (MCP), and a phosphor layer. The photons incident on the photocathode are converted into photoelectrons (quantum efficiency  $\eta_{PC} \sim 3.8\%$  at 750 nm down to  $\sim 0.46\%$  at 850 nm, with a decay close to exponential, as specified for the photocathode material S20). A fraction  $\Omega \sim 60\%$  of these photoelectrons actually enter the MCP active area. Secondary photoelectrons are produced and multiplied in the MCP with a gain  $G_{MCP}$  depending on the high voltage  $V=260\text{--}800$  V applied to the MCP. They are then accelerated toward a phosphor layer where they produce green photons. A 2:1 lens system insures the relay to the CCD array (efficiency  $\eta_{Relay} \sim 5\%$ ), where the green photons are converted into photoelectrons (quantum efficiency  $\eta_{CCD} \sim 70\%$ ) and stored in wells for the specified integration time  $\tau$ . The total sensitivity of the ICCD was calculated using the photocathode quantum efficiency and the MCP sensitivity provided by the manufacturer and is shown in Fig. 3(a) at  $\lambda=800$  nm. The actual sensitivity depends on additional parameters, such as the incident wavelength and the CCD pixel binning, and is affected by saturation effects at high powers and MCP gains (up to 50% loss at high power for  $V=800$  V). See Ref. 30 for a more systematic description of all the mentioned effects.

The signal is affected by noise from the image intensifier and from the CCD camera, with a strong dependence on the ICCD gain. Sources of noise include intensifier shot noise, dark noise, noise resulting from the gain process in the MCP, phosphor photon shot noise, CCD dark noise, and CCD read-out noise. Brukilacchio shows a dependence of the SNR on the signal as being close to a square root,<sup>30</sup> with saturation effects appearing at high signal levels.

We measured experimentally the SNR as a function of the number of CCD counts for different values of the intensifier gain (see Fig. 3(b)). The probe was set on a solid scattering phantom with optical properties  $\mu_a \sim 0.085 \text{ cm}^{-1}$  and  $\mu_s \sim 4.9 \text{ cm}^{-1}$  at 800 nm, and CCD frames with 100-ms integration time were acquired at  $\sim 8$  Hz for 1 minute. Two hundred dark frames were also recorded with the laser beam blocked, and the averaged dark image was subtracted from the previous signal images. The dark signals from the MCP and the CCD are around 40 to 50 counts per frame. The process was repeated for various intensities of the source by varying the attenuation of the incident beam. We defined the signal as the

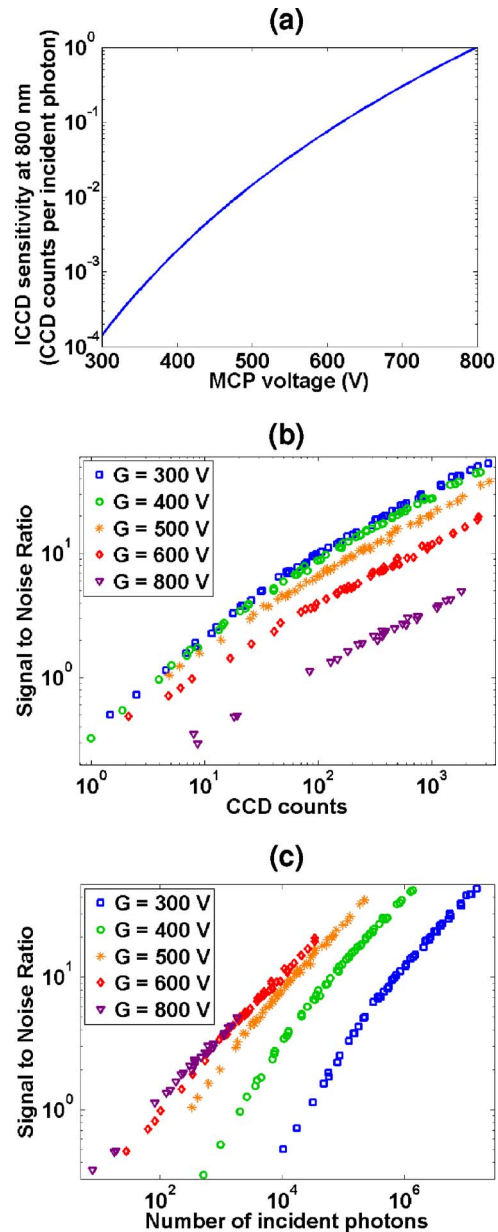


**Fig. 3** (a) ICCD sensitivity at 800 nm as a function of the MCP voltage, deduced from the manufacturer indications. (b) Experimental SNR vs. number of CCD counts, for different MCP voltages. (c) Signal to noise ratio vs. number of incident photons, as deduced from the two previous curves.

number of CCD counts on one pixel for each detector fiber corrected by the dark image, averaged over all the recorded frames. The noise was defined as the standard deviation of this value. The evolution of the SNR with the number of counts is very close to a square root. For typical signal values encountered in our functional imaging experiments ( $\tau = 100$  ms;  $V=500\text{--}800$  V) with pixel counts close to saturation, we thus expect the SNR to vary between 3 and 50. These values can be improved by integrating the signal over more pixels. A factor of 2 in the SNR can be gained by averaging the signal over 10 pixels, after which the SNR reaches saturation. We would expect an improvement of the SNR as the

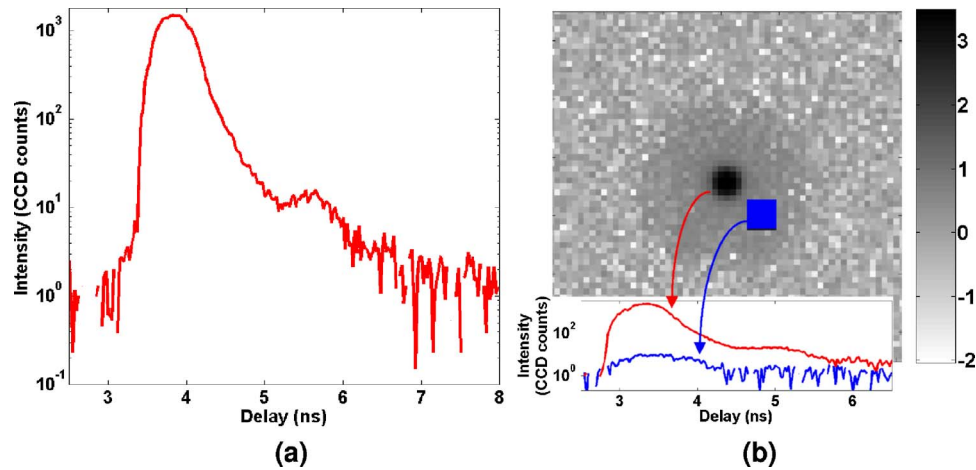


**Fig. 4** (a) Typical instrumental response function (IRF) of the instrument, measured for one source fiber and one detector fiber facing each other with a diffusive paper between them. A typical secondary peak due to glass reflection from the camera is visible  $\sim 1800$  ps after the main peak. (b) Typical cross-talk between detector fibers. The decimal logarithm of the intensity on the CCD is shown for a single illuminated fiber. The square indicates the position of the nearest detector fiber. The insert shows the signal evolution for the region of interest corresponding to the central fiber, and for the nearest fiber.

square root of the number of averaged pixels if the signal and noise were of the same magnitude on each pixel, and the noise was uncorrelated. However, not all pixels from the region of interest have the same signal level, which explains the saturation in SNR as we increase the number of pixels in the estimate of the signal.

From the ICCD sensitivity and the experimental SNR, we deduced the evolution of the SNR with the number of incident photons (Fig. 3(c)). For a given number of incident photons, the SNR increases with increased gain, within the saturation limit of the CCD.

### 3.3 Instrument Response Function

When measuring an experimental TPSF on a phantom or a head, the system records the true TPSF due to the optical properties of the medium, convolved by the instrument response function (IRF). The IRF accounts for the laser pulse width, the width and shape of the detector gate, the pulse broadening in the source and detector fibers, and additional electronic delays. It is therefore important to empirically determine the width and shape of the IRF. We estimated this by placing a source fiber and a detector fiber facing each other 1 cm apart with a diffusive paper between them, as was suggested by Liebert et al. to fill all the fiber modes.<sup>31</sup> The source intensity was greatly attenuated with the exit polarizer to avoid detector saturation. A resulting IRF is shown in Fig. 4(a) for a gate width set to 300 ps. The measured FWHM is about 500 ps, which can be explained by the dispersion in the fibers (in this case, 3 meters of source fiber and 3 meters of detector fiber). A characteristic secondary amplitude peak of about 1% of the maximum is visible about 1800 ps after the primary peak. This secondary peak is due to reflection of light on the photocathode and back on the fiber array. The 1800-ps delay corresponds to an optical path of about 36 cm in glass, which is twice the length of the camera lens.

### 3.4 Cross-Talk

The cross-talk between detectors or between sources and detectors is a crucial point to characterize as it can affect the measurements greatly. There are two main possible mechanisms for cross-talk in our system: source to detector, and detector to detector. The source to detector fiber cross-talk has to be carefully controlled, as the light intensity in the source fibers can be 9 to 12 orders of magnitude higher than the light intensity in the detector fibers. Even an extremely small fraction of light leaking from source to detector fiber would cause high distortion of the signal. To prevent that effect, we shielded all sources and detector fibers in black PVC insulating tubing. This also prevents detector to detector cross-talk along the fibers. However, all fibers are imaged in parallel on the same CCD array, which we identified as the main cause for detector cross-talk. Fig. 4(b) shows the spot created by one illuminated fiber on the CCD array after background subtraction. Intensity is displayed in decimal log to visualize low CCD counts. The spot extends to a larger area than the pixels taken into account for this fiber, and in particular it covers the area of the next closer fiber (indicated by the square). The TPSF measured on the central fiber and on the closest one are presented in the figure insert. A cross-talk of about 0.3% is visible at the peak of the TPSF. At later delays, the difference between the two curves decreases as we reach the background noise level.

### 3.5 Stability and Reproducibility

We characterized the stability and reproducibility of our system by measuring the evolution of the IRF over time for a single source-detector.

The stability of the signal was measured over 10 minutes, which is the typical duration of a single run for functional imaging. Two kinds of variations are observed simultaneously when studying the stability: the intensity stability and the stability of the temporal delay. To minimize the effects of a delay

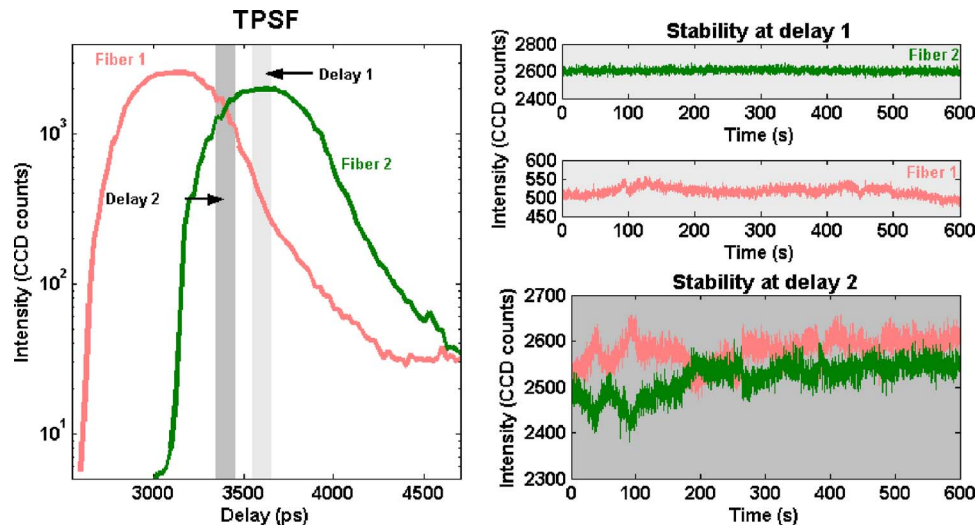


**Fig. 5** Stability measurements. (a) TPSF recorded at the two fibers where the stability was measured (same detector bundle, two fibers of different lengths). The two gray areas show the delay gates at which the stability was assessed. The actual gate width is wider than represented. (b) Stability over 10 min measured at delay 1. Note in particular fiber 2 for which the slope of intensity vs. delay is close to zero, and which presents very little intensity variation over time. On the contrary, the intensity from fiber 1 (high slope intensity vs. delay) presents several percent variation over 10 min, due to delay drifts. (c) Stability over 10 min measured at delay 2, for fibers 1 and 2.

drift, we first made a measurement at the peak of the IRF, where the slope of intensity vs. delay is close to zero (see Fig. 5(a), fiber 2 at delay 1). In that case, the intensity variations were found to be less than 0.6% over 10 minutes (Fig. 5(b), fiber 2). When the measurement is made at a delay where the IRF slope is high, this stability can deteriorate to 5–10% variation over 10 minutes (Fig. 5(b), fiber 1, and Fig. 5(c)). The instabilities shown in Fig. 5(c) are clearly due to variations in the delay, evidenced by the correlated signal changes of opposite directions in the two delay windows where the slopes have opposite directions. Taking into account the slope of the IRF at this delay, the 10% variation corresponds to a delay variation of about 30 ps. Even though the delay drift is small, it causes significant intensity variations, much larger than the intensity changes we expect to detect during functional brain imaging. However these variations related to delay drifts are slow (typical time scale  $\sim 1$  minute) and can be removed by our standard 0.02 Hz high-pass filtering of brain activation data.

The reproducibility was estimated by repeating measurements at intervals of several hours. The delay variations were found to be less than 100 ps over several days. However, the drifts in intensity or delay in this case is not a very relevant parameter, since such drifts would not interfere with the measurements as functional imaging experiments typically last for no more than several minutes. As for characterization of optical properties of a medium, we always first measure a reference phantom to calibrate the system. To estimate the reproducibility of the system, we thus proceeded differently: we repeated the measurement of the absolute optical properties of a scattering phantom as described in Section 4 (see ahead). For each characterization, we first measured a reference phantom to determine the IRF, we then measured the target phantom. Over five hours, the maximum variation in the measured  $\mu_a$  was 5%, and 13% for  $\mu'_s$ .

#### 4 Fitting of Baseline Optical Properties

The TD system can be used to estimate the absolute optical properties ( $\mu_a$  and  $\mu'_s$ ) of a tissue by nonlinear regression of the measured TPSF to a theoretical model.<sup>32–36</sup> As mentioned previously, the measured TPSF is the convolution of the true TPSF of the medium convolved by the IRF.<sup>37,38</sup> We extract the IRF by deconvolution of a reference TPSF measured on a calibration phantom of known optical properties, which were obtained from cross-validated measurements by other systems in our laboratory, in particular a frequency-domain instrument (*ISS Imagent*).<sup>39</sup> This procedure gives us the shape of the IRF (and in particular its width) as well as the initial delay  $t_0$  relative to the pulse emission.

We use a nonlinear regression procedure based on a Levenberg-Marquardt algorithm with two fitting parameters ( $\mu_a$  and  $\mu'_s$ ). Our forward model is the analytical solution of the diffusion equation for a semi-infinite homogeneous medium,<sup>32</sup> with extrapolated boundary conditions.<sup>33</sup> The fit is simultaneously performed at two distances. The measured TPSF is fitted within the delay range delimited by data corresponding to 50% of the maximum value on the rising edge, and 0.5% on the tail. For each step of the nonlinear fitting routine, the analytical TPSF is calculated for the updated optical properties, then convolved by the experimental IRF. An independent amplitude factor is fitted for each detector to account for the fiber coupling and instrumental differences between channels. A logarithmic cost function is used to give equal weight to all points of the TPSF.

As presented, e.g., by Abrahamsson et al., the cost function presents a narrow elliptical shape in the ( $\mu_a$ ,  $\mu'_s$ ) space,<sup>35</sup> which is responsible for high cross-talk between absorption and scattering. Furthermore, the scattering coefficient is highly dependent on the initial delay  $t_0$  relative to the pulse emission, as an increased  $t_0$  can be compensated in the fitting

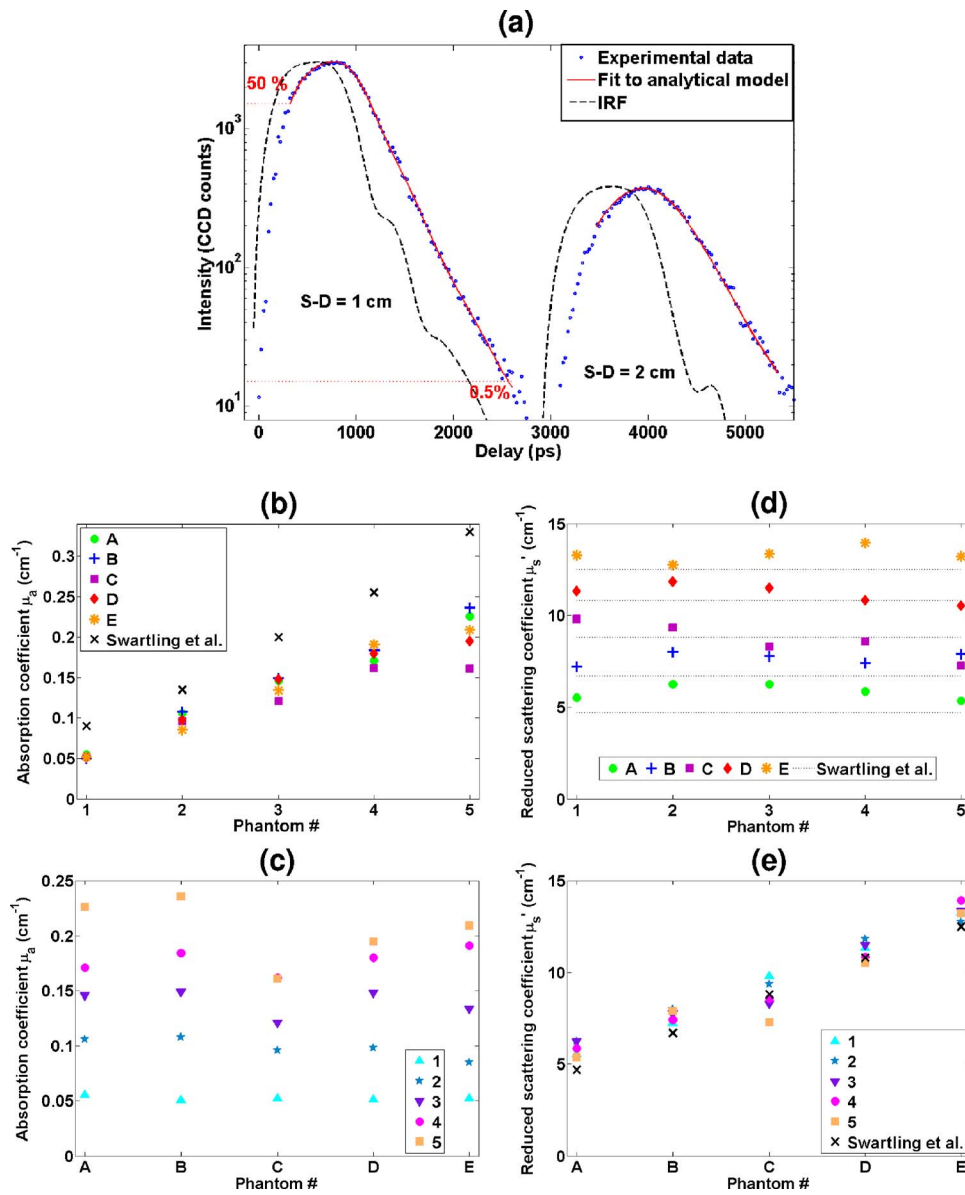


**Fig. 6** Fitting of baseline optical properties. (a) Experimental TPSFs for source–detector separations of 1 and 2 cm (gate width=800 ps), and best fit to analytical model. Also shown are the normalized deconvoluted IRFs (dashed curves) used for the fitting; note that the amplitude information is not used. (b–c) Fitted absorption coefficients of the phantoms for increasing  $\mu_a$  (b) and increasing  $\mu'_s$  (c). (d–e) Fitted scattering coefficients of the phantoms for increasing  $\mu_a$  (d) and increasing  $\mu'_s$  (e). The values estimated by Swartling et al.<sup>36</sup> on the same phantoms with an integrating sphere are shown as crosses (×) or dotted lines. For the absorption, they averaged the coefficients over phantoms A to E (same nominal  $\mu_a$ ), and for the reduced scattering, they averaged over phantoms 1 to 5 (same nominal  $\mu'_s$ ).

process by a lower  $\mu'_s$ . Even an error of only 50 ps on  $t_0$  is responsible for a change in  $\mu'_s$  of the order of 1  $\text{cm}^{-1}$ . The calibration of  $t_0$  is therefore a critical point of the fitting, as an error on  $t_0$  will propagate as an error on  $\mu'_s$ , which can in turn influence  $\mu_a$  in the same direction. However the calibration of  $t_0$  on a phantom is difficult, since we observed that  $t_0$  can drift during the course of an experiment (see Fig. 5(c)). We found the following procedure to give more robust results: we first fit for  $\mu_a$  and  $\mu'_s$  with  $t_0$  imposed from the IRF measurement. The  $\mu_a$  and  $\mu'_s$  results are then used as initial guesses for a second fit where  $t_0$  is also a fit parameter at each step, with a constraint of  $\pm 50$  ps around the previous value for  $t_0$ . Based

on our stability measurements, we estimate that no drift higher than 50 ps in each direction would occur during the course of an experiment.

We validated the fitting procedure on a set of 25 solid epoxy tissue phantoms provided by Prof. Andersson-Engels from Lund Institute of Technology, Sweden.<sup>36</sup> The optical properties of the phantoms span all combinations of 5 absorption coefficients and 5 scattering coefficients. The resulting 25 phantoms are called A1, B1, C1, D1, E1 to A5–E5, where a same letter indicates a same scattering coefficient, and a same number means a same absorption coefficient. We used a probe consisting of one source and two detectors, at distances 1 and



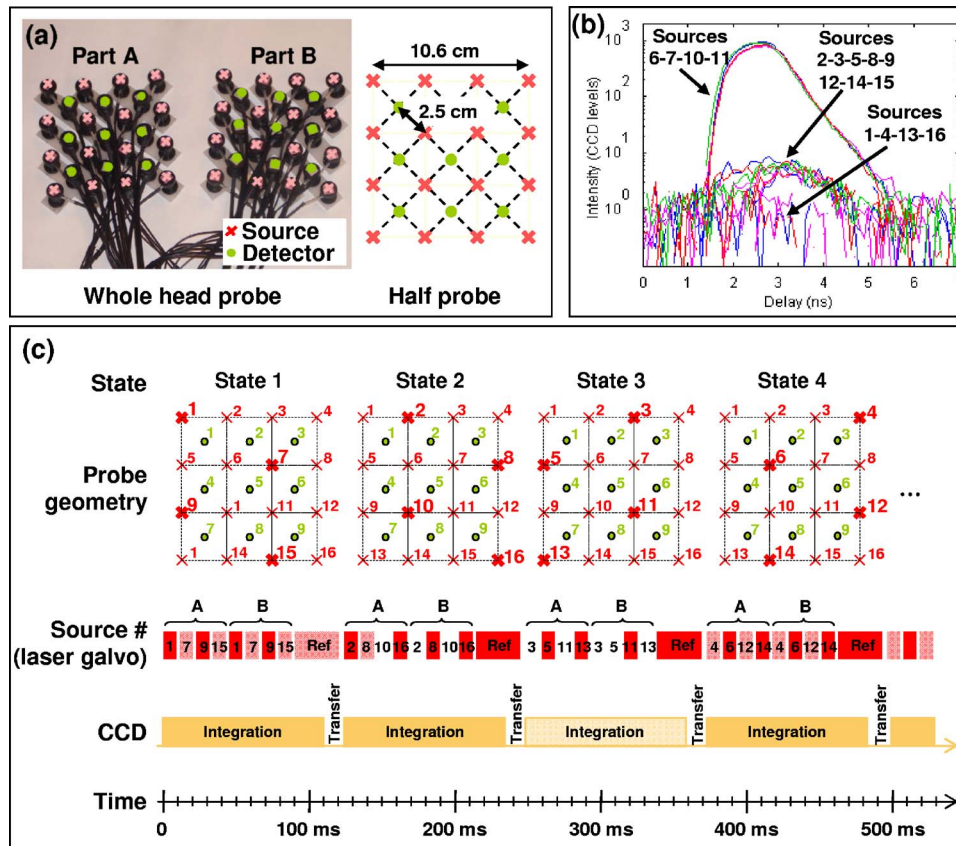


**Fig. 7** Two-hemisphere imaging. (a) Two-part probe picture. (b) TPSFs detected on detector 5 for successive illumination of sources 1 to 16. (c) Schematic showing the principle of the source scanning.

2 cm. Figure 6(a) shows a typical fit for the two source–detector separations. Figures 6(b)–6(e) show the results of the fitting for  $\mu_a$  and  $\mu'_s$  at 785 nm, for simultaneous fitting of the TPSFs at the two separations. These absolute values are in reasonable agreement with those obtained by Swartling et al. on the same phantoms,<sup>36</sup> and shown on the same graphs. Specifically, our absorption coefficients are about 25 to 35% lower than theirs, while the reduced scattering coefficients agree within 15% or better. Note that our results depend strongly on the optical properties we assess for the reference phantom. The results show good linearity with  $\mu_a$  and  $\mu'_s$  and relatively low cross-talk, with the exception of subset C. We believe that a drift of  $t_0$  higher than what our routine accounts for is responsible for the error in subset C.

## 5 Application for Functional Brain Imaging

The main application of the system is depth-resolved functional brain imaging. We have demonstrated the depth sensitivity of our system previously<sup>18</sup> with a simple one-source probe located on the subject's motor cortex. This improved instrument now has 42 time-multiplexed sources, and 175 detector fibers (25 positions with 7 delayed fibers each). The large number of source and detector fibers allows a wide variety of probe geometries. We have developed a probe that covers both hemispheres with a source multiplexing enabling 1.8 Hz imaging with 32 sources and 18 detectors (126 detector fibers). In this part, we describe the implementation of the

1.8 Hz two-hemisphere acquisition and show images on dynamic phantoms as well as preliminary human data.

### 5.1 Head Probe

The head probe is divided into two parts, one for each hemisphere (see Fig. 7(a)). Each half consists of  $4 \times 4$  sources and  $3 \times 3$  detectors (7 delays each) in a square geometry, with a source–detector separation of 2.5 cm. This separation was chosen to enable good coverage of the whole head while maintaining an acceptable SNR. The fixation of the fibers on the head is achieved in a way common to most functional brain imaging equipment in our laboratory. For the detector fibers, the tips of each group of 7 fibers are inserted in a 3-cm-long metallic ferrule bent at 90 degrees with a smooth curvature (custom made). For the source fiber, the same process is used with only one fiber per ferrule. The ferrule is spring-loaded in a plastic optode cap. These plastic optodes in turn plug into the slots made on the head probe. The probe itself is made out of soft plastic and Velcro bands to attach onto a headband fixed around the head. The whole probe can be further secured with a chinstrap. On the detector side, all 175 fibers were epoxied together in a circular plug and polished simultaneously. The plug is inserted in front of the lens that forms its image onto the ICCD.



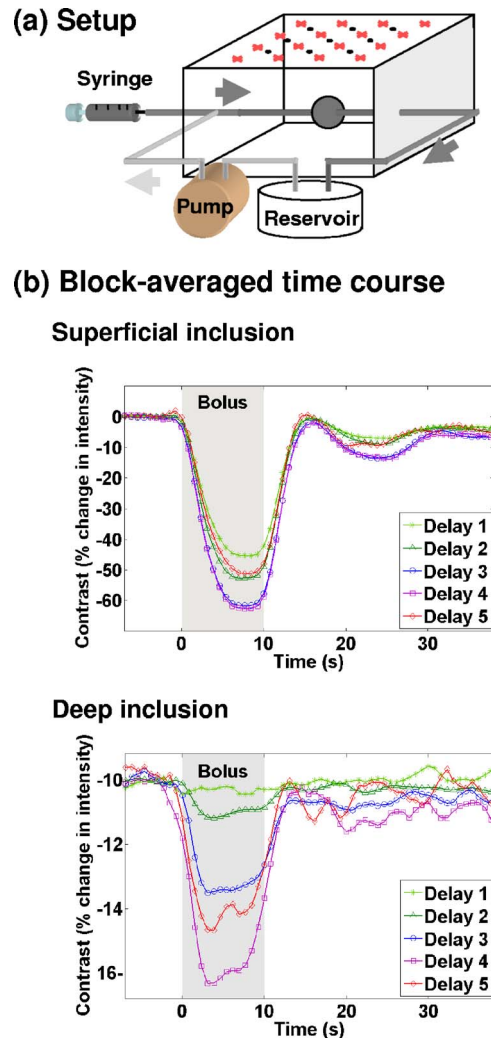
## 5.2 Source Scanning

On the source side, we only have one light source: we need to time-multiplex it to illuminate the 32 source fibers sequentially. We thus divided the 32 source positions into 4 subsets of 8 sources that can be illuminated during the same camera frame while minimizing cross-talk from second nearest sources (see first line of Fig. 7(c)). For each subset, each detector only sees one of its nearest neighbor sources, the other sources being turned off. During one camera frame lasting 100 ms, we scan the galvanometer mirror through the 8 positions, staying approximately 10 ms on each, then switching to a reference fiber. The timing scheme of this scanning is illustrated in Fig. 7(c). The reference fiber goes to a photodiode whose output is low-pass filtered and compared to a reference signal. The comparator controls a switch that closes the laser interlock in case the scanning fails and thus avoids excessive integrated laser power on the subject's scalp. The source scanning and safety device enable us to increase the power at the end of the source fibers. The mean power at the end of each fiber was set to 100 mW, which corresponds to an average power of 2 mW because of the 2% duty cycle (each fiber shines light during 11 ms every 556 ms). Because of scattering, the effective diameter of the light illumination can be considered to be 3 mm at this wavelength, leading to a power density of  $\sim 28$  mW/cm<sup>2</sup>, well below the ANSI safety standards for skin exposure at these wavelengths (250 to 400 mW/cm<sup>2</sup> from 750 to 850-nm). By defining 4 illumination states corresponding to one camera frame each, we reduce the acquisition frequency by a factor of 4. This yields an effective acquisition frequency for the whole head of  $\sim 1.8$  Hz, which is reasonable for functional imaging.

When the source scanning is implemented, the system stability over 10 minutes deteriorates to approximately 1%, when care is taken not to measure the delay drifts (see the procedure for stability measurement above). We studied the cross-talk from second nearest sources by placing the probe on a scattering phantom of optical properties  $\mu_a \sim 0.085$  cm<sup>-1</sup> and  $\mu'_s \sim 4.9$  cm<sup>-1</sup>. We turned each source on alternatively, and recorded the complete TPSF for all detectors. One result is presented for detector 5 in Fig. 7(b). For better clarity we show only the signal recorded by one of the 7 detector fibers. Note that the curves were plotted without any delay or amplitude correction, showing very good precision in the probe construction. Second-nearest-neighbor sources are visible with an amplitude about 1% of that of the nearest neighbor. For simultaneous illumination of all sources of a particular state, this distinction between nearest and second-nearest sources could not be made, leading to some cross-talk between sources. However, this cross-talk was smaller when measured on the head of a volunteer, between 0.2% and 1% depending on the detector position. This smaller cross-talk is probably due to the fact that the head is more absorbing and scattering than the phantom. The variation between detectors can be explained by the fact that the source-detector separations are less accurate on the curved head.

## 5.3 Dynamic Imaging on Phantoms

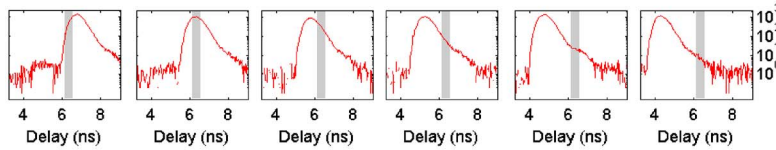
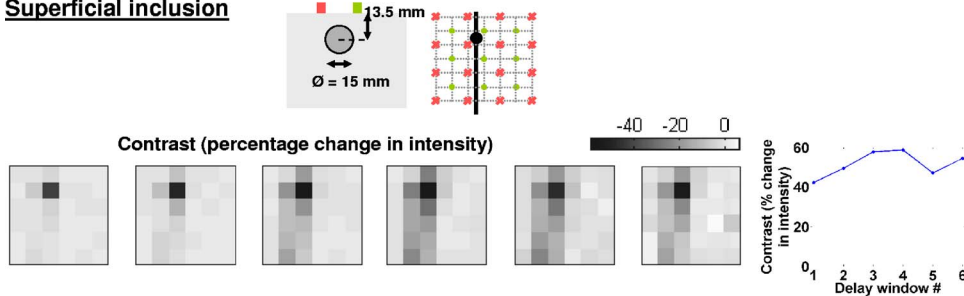
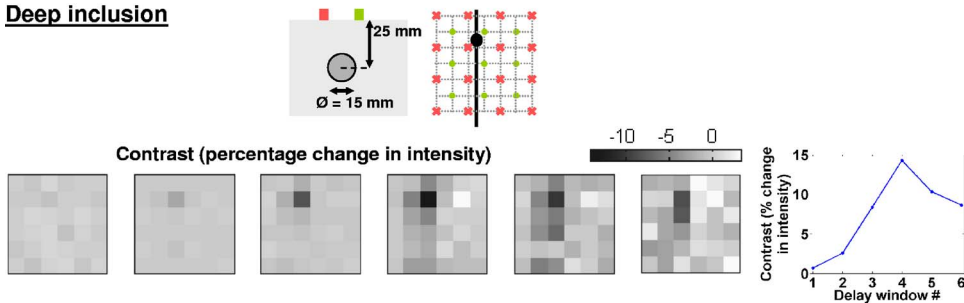
The real-time acquisition capability of the system was tested on dynamic liquid phantoms. The setup is shown Fig. 8(a). The phantom consisted of a 19 cm  $\times$  19 cm  $\times$  9 cm tank



**Fig. 8** (a) Dynamic phantom setup. (b) Block-averaged time course of the intensity changes for the source-detector pair of maximal contrast, for a superficial (left) and a deep (right) inclusion.

filled with a solution of intralipid and ink. A 15-mm diameter hollow glass sphere connected to horizontal tubes was embedded in the middle of the tank and filled with the same solution. A mechanical pump allowed circulation of the solution through the tubes via a 2 L reservoir. At one extremity, one of the tubes was also connected through a derivation to a 50-mL syringe containing the same intralipid solution but with increased ink concentration to create a higher absorption coefficient. Every 40 sec, 10 mL of the darker solution was injected in the tube over a period of 10 sec. The pump circulated this ink bolus into the sphere, after which it was diluted in the reservoir. The ink bolus created a transient absorption contrast in the sphere roughly similar to brain activation. Five boli were injected successively, enabling a block-averaging of the data as usually done in brain function experiments. We performed this experiment with the sphere at two different depths: top of the sphere at 6 mm and 17.5 mm below the surface.

By fitting the TPSFs measured before the dynamic experiment to an analytical model, as described in part 4 above, we

**Delay window****Superficial inclusion****Deep inclusion**

**Fig. 9** Contrast maps of the dynamic phantoms. The first line shows the delay window in which each map was made. The second and third lines show the averaged contrast maps for a superficial and deep inclusion, respectively (each pixel corresponds to a source–detector pair). The last curve of each line presents the evolution of the contrast with the delay for the pixel of maximum contrast.

estimated the following optical properties for the liquid phantom at 830 nm:  $\mu_a = 0.14 \text{ cm}^{-1}$  and  $\mu'_s = 10.2 \text{ cm}^{-1}$ . We did not estimate the optical properties of the solution used for the bolus, which had a very high absorption coefficient. The ink concentration was about 70 times higher in the bolus than in the background.

Figure 8(b) shows the evolution of intensity with time at five different delays for the source–detector pair above the sphere, after averaging over the five successive blocks, for the superficial inclusion (top) and the deep inclusion (bottom). The curves at the last two delays are not shown because of a high noise level. Even though we are only showing one source–detector pair measurement, note that data from all 36 source–detector pairs (72 if we use both sides of the probe) were acquired in parallel at 1.8 Hz. For the superficial inclusion, the curves are very similar at every delay, the contrast increasing only very slightly for late delays. We attribute the secondary dip in the intensity time course to incomplete mixing of the ink bolus in the reservoir: the ink bolus therefore goes twice through the sphere, though with a lower absorption the second time. Also, note that the block averaged signal does not recover to zero level at 35 sec after bolus injection in the case of the superficial inclusion, because the successive injected boli, even though diluted in the reservoir, gradually increased the average absorption coefficient of the solution in the sphere, resulting in an overall decrease in intensity. For the deep inclusion, the change in the intensity increases as we

increase the delay as expected and described in Ref. 18.

From each time course, we define the contrast as the change in intensity between the *off* state (before ink injection) and the *on* state (during ink injection). This contrast is calculated for each source–detector pair and each delay window. Figure 9 shows the resulting contrast maps for 5 different delay windows represented on the first line. For a superficial inclusion (2nd row), the inclusion is visible from the first delay window, and its contrast only increases mildly with delay. On the contrary, for a deep inclusion (3rd row), the contrast of the inclusion is almost null in the first window, and its contrast increases to become maximum in the fourth delay window. In both cases, the tubes themselves are also visible, due to their rather large diameter (3 mm). Also, note that the scales of the contrast maps are different in the two cases: the superficial inclusion yields a higher contrast than the deep one. As we had previously predicted theoretically,<sup>18</sup> the two depths of inclusion give rise to very different behavior for the evolution of contrast with delay (see last curve of each line on Fig. 9).

#### 5.4 Human Results

As a last step of validation, we tested the imaging system on a healthy 34-year-old volunteer during a motor stimulus. The study was approved by the Institutional Review Board of Massachusetts General Hospital, and the subject gave in-

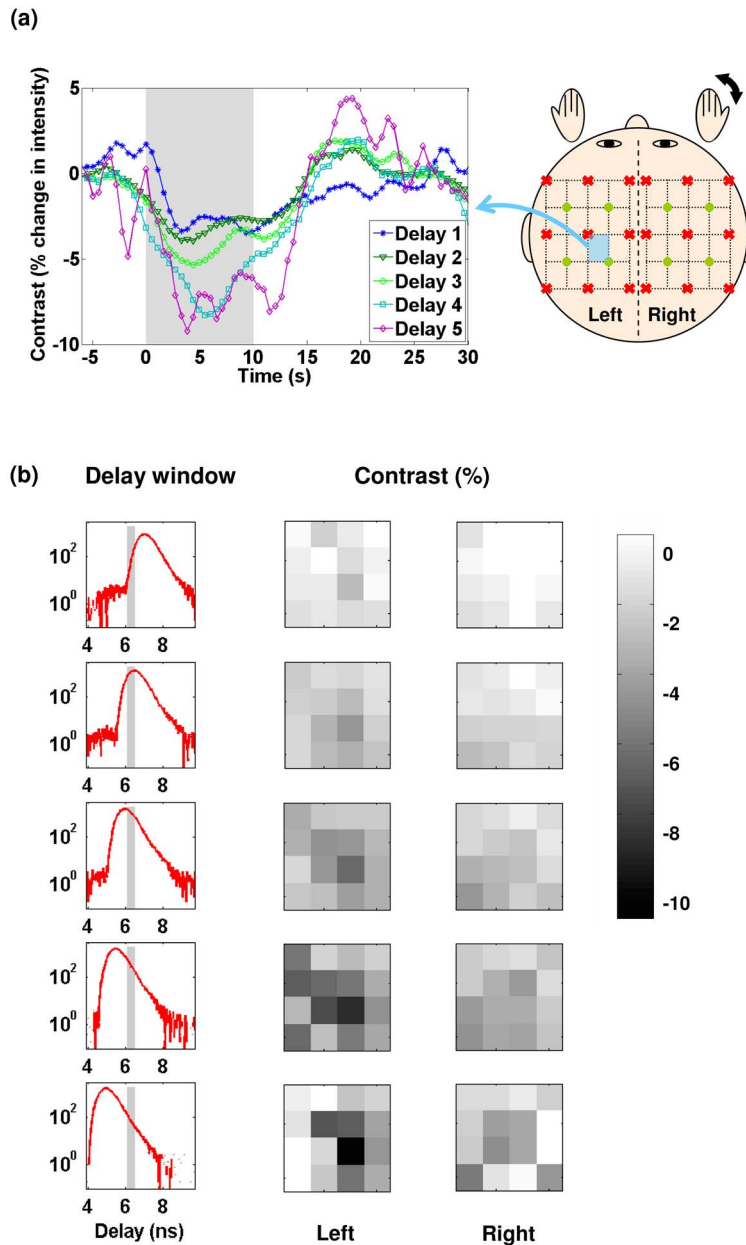


**Fig. 10** Functional brain imaging on an adult volunteer. (a) Time course of the block-averaged intensity changes for the source–detector pair of maximal contrast. (b) Contrast maps for the left and right hemispheres, at the delay windows shown in the first column.

formed written consent. The stimulus was a self-paced finger-tapping of the right hand. The subject was reclined, and instructed to touch the thumb with all other fingers of the hand alternatively. The protocol consisted of 20 blocks of alternate finger-tapping (10 sec) and resting (20 sec), for a total run time of 10 min. We repeated the whole run three times. For this preliminary experiment, we used a simplified version of the probe, to make its positioning easier. Each half of the probe consisted of only  $3 \times 3$  sources and  $2 \times 2$  detectors, for a total of 18 sources and 8 detectors on the head, and a source–detector separation of 3 cm. The imaging was done at  $\lambda = 830$  nm. The raw intensities were low-pass filtered (moving average filter over a 2-sec window) to remove heart beat oscillations and high-frequency noise, and slow drifts of the

signal were subtracted (moving average filter over a 50-sec window). Block averaging over 18 successive blocks of each run was then performed, the first and last block of each run being removed to avoid artifacts due to the filtering process.

Figure 10(a) shows the time course of the block-averaged intensity for the first run, obtained on the source–detector pair of maximum contrast, on the hemisphere contralateral to the hand tapping, at 5 different delays. The tapping duration is indicated by the gray area. We observe a response to the stimulus (decrease in intensity) from the first delay window, indicating some contribution from the superficial layers. However, the contrast increases with delay, and the time course of the response varies with delay, showing that a deeper response is also present. When considering the time courses of all



source–detector pairs (data not shown), we observe the small response in the early windows on most of them, but the strong increase of the contrast with delay is only present locally.

To present the results over both hemispheres, we calculated the contrast maps as done with the dynamic phantom (see Fig. 10(b)). The “on” time is defined between 5 sec and 10 sec after the stimulus onset, the “off” time between 17 sec and 25 sec. In the left hemisphere, contralateral to the tapping hand, a localized response is observed in-depth, as indicated by the strong increase in contrast with delay. A smaller ipsilateral response is also observed. Note that almost all pixels show some contrast, though much smaller than the localized response, and almost constant with delay. We interpret this as a systemic response, yielding a change in the skin, thus visible over the whole head. Previous theoretical and experimental work shows that superficial response yields almost uniform contrast with delay.<sup>18</sup>

## 6 Conclusion

We developed and characterized a time-gated optical system for functional brain imaging. The performance of the system was studied in terms of instrument response, signal-to-noise ratio, cross-talk, stability, and repeatability. Because this system is capable of two operation modes, it was used for two different applications: characterization of baseline optical properties of homogenous phantoms, and real-time functional imaging of the human head. For the latter application, we confirmed previous results showing depth discrimination of the system, now combined with 1.8 Hz imaging of both hemispheres.

### Acknowledgments

We would like to acknowledge Tom Brukilacchio and Jonathan Stott for the initial development of the time-domain system and the control software. We are also grateful to Tom Brukilacchio for the extensive noise model and characterization provided in his Ph.D. thesis. We would like to thank Ilkka Nissilä and Theodore Huppert for their useful comments on the manuscript. We are grateful to Stefan Andersson-Engels for lending us the set of phantoms used to validate the fitting procedure.

We acknowledge funding by the U.S. National Institute of Health (N.I.H.) Grants National Center for Research (NCR) P41-RR14075, National Institute of Biomedical Imaging and Bioengineering (NIBIB) RO1-EB002482, and RO1-HD42908.

### References

1. A. Villringer, J. Planck, C. Hock, L. Schleinkofer, and U. Dirnagl, “Near infrared spectroscopy (NIRS): A new tool to study hemodynamic changes during activation of brain function in human adults,” *Neurosci. Lett.* **154**, 101–104 (1993).
2. Y. Hoshi and M. Tamura, “Detection of dynamic changes in cerebral oxygenation coupled to neuronal function during mental work in man,” *Neurosci. Lett.* **150**, 5–8 (1993).
3. J. C. Hebden, S. R. Arridge, and D. T. Delpy, “Optical imaging in medicine: I. Experimental techniques,” *Phys. Med. Biol.* **42**, 825–840 (1997).
4. H. Obrig and A. Villringer, “Beyond the visible—imaging the human brain with light,” *J. Cereb. Blood Flow Metab.* **23**, 1–18 (2002).
5. A. P. Gibson, J. C. Hebden, and S. R. Arridge, “Recent advances in diffuse optical imaging,” *Phys. Med. Biol.* **50**, R1–R43 (2005).
6. M. A. Franceschini, S. Fantini, J. H. Thompson, J. P. Culver, and D.

- A. Boas, “Hemodynamic evoked response of the sensorimotor cortex measured non-invasively with near-infrared optical imaging,” *Psychophysiology* **40**, 548–560 (2003).
7. M. A. Franceschini, V. Toronov, M. E. Filiaci, E. Gratton, and S. Fantini, “On-line optical imaging of the human brain with 160-ms temporal resolution,” *Opt. Express* **6**, 49–57 (2000).
8. J. H. Meek, C. E. Elwell, M. J. Khan, J. Romaya, J. S. Wyatt, and D. T. Delpy, “Regional changes in cerebral haemodynamics as a result of a visual stimulus measured by near infrared spectroscopy,” *Proc. Biol. Sci.* **261**(1362), 351–356 (1995).
9. T. Wilcox, H. Bortfeld, R. Woods, E. Wruck, and D. A. Boas, “Using near-infrared spectroscopy to assess neural activation during object processing in infants,” *J. Biomed. Opt.* **10**(1), 11010 (2005).
10. K. Kotilahti, I. Nissilä, M. Huottilainen, R. Mäkelä, N. Gavrielides, T. Noponen, P. Björkman, V. Fellman, and T. Katila, “Bilateral hemodynamic responses to auditory stimulation in newborn infants,” *NeuroReport* **16**(12), 1373–1377 (2005).
11. E. Watanabe, A. Maki, F. Kawaguchi, K. Takashiro, Y. Yamashita, H. Koizumi, and Y. Mayanagi, “Non-invasive assessment of language dominance with near-infrared spectroscopic mapping,” *Neurosci. Lett.* **256**, (1), 49–52 (1998).
12. D. A. Boas, A. M. Dale and M. A. Franceschini, “Diffuse optical imaging of brain activation: approaches to optimizing image sensitivity, resolution and accuracy,” *Neuroimage* **23**, S275–S288 (2004).
13. Y. Zhang, D. H. Brooks, M. A. Franceschini, and D. A. Boas, “Eigenvector-based spatial filtering for reduction of physiological interference in diffuse optical imaging,” *J. Biomed. Opt.* **10**(1), 011–014 (2005).
14. V. Toronov, M. A. Franceschini, M. E. Filiaci, M. Wolf, S. Fantini, and E. Gratton, “Near-infrared study of fluctuations in cerebral hemodynamics during rest and motor stimulation: spatial mapping and temporal analysis,” *Med. Phys.* **27**, 801–815 (2000).
15. M. Kohl-Bareis, H. Obrig, J. Steinbrink, J. Malak, K. Uludag, and A. Villringer, “Noninvasive monitoring of cerebral blood flow by a dye bolus method: Separation of brain from skin and skull signals,” *J. Biomed. Opt.* **7**(3), 464–470 (2002).
16. J. Steinbrink, H. Wabnitz, H. Obrig, A. Villringer, and H. Rinneberg, “Determining changes in NIR absorption using a layered model of the human head,” *Phys. Med. Biol.* **46**(3), 879–896 (2001).
17. A. Liebert, H. Wabnitz, J. Steinbrink, H. Obrig, M. Moller, R. Macdonald, A. Villringer, and H. Rinneberg, “Time-resolved multidistance near-infrared spectroscopy of the adult head: Intracerebral and extracerebral absorption changes from moments of distribution of times of flight of photons,” *Appl. Opt.* **43**(15), 3037–3047 (2004).
18. J. Selb, J. J. Stott, M. A. Franceschini, A. G. Sorenson, and D. A. Boas, “Improved sensitivity to cerebral dynamics during brain activation with a time-gated optical system: Analytical model and experimental validation,” *J. Biomed. Opt.* **10**(1), 011–013 (2005).
19. B. Montcel, R. Chabrier, and P. Poulet, “Detection of cortical activation with time-resolved diffuse optical methods,” *Appl. Opt.* **44**(10), 1942–1947 (2005).
20. H. Eda, I. Oda, Y. Ito, Y. Wada, Y. Oikawa, Y. Tsunazawa, M. Takada, Y. Tsuchiya, Y. Yamashita, M. Oda, A. Sassaroli, Y. Yamada, and M. Tamura, “Multichannel time-resolved optical tomographic imaging system,” *Rev. Sci. Instrum.* **70**, (9), 3595–3602 (1999).
21. H. Wabnitz, M. Moeller, A. Liebert, A. Walter, R. Erdmann, O. Raitza, C. Drenckhahn, J. P. Dreier, H. Obrig, J. Steinbrink, and R. Macdonald, “A time-domain NIR brain imager applied in functional stimulation experiments,” in *Photon Migration and Diffuse-Light Imaging II*, K. Licha and R. Cubeddu, Eds., *Proc. SPIE* **5859**, 58590H (2005).
22. J. C. Hebden, A. Gibson, T. Austin, R. Md. Yusof, N. Everdell, D. T. Delpy, S. R. Arridge, J. H. Meek, and J. S. Wyatt, “Imaging changes in blood volume and oxygenation in the newborn infant brain using three-dimensional optical tomography,” *Phys. Med. Biol.* **49**, 1117–1130 (2004).
23. D. Contini, A. Pifferi, L. Spinelli, A. Torricelli, and R. Cubeddu, “Design and characterization of a fast 16-source 64-detector time-resolved system for functional NIR studies,” in *Photon Migration and Diffuse-Light Imaging II*, K. Licha and R. Cubeddu, Eds., *Proc. SPIE* **5859**, 58590U (2005).
24. B. Montcel, R. Chabrier, and P. Poulet, “Improvements in brain activation detection using time-resolved diffuse optical means,” in *Photon Migration and Diffuse-Light Imaging II*, K. Licha and R. Cubeddu, Eds., *Proc. SPIE* **5859**, 58590G (2005).

25. F. E. W. Schmidt, M. E. Fry, E. M. C. Hillman, J. C. Hebden, and D. T. Delpy, "A 32-channel time-resolved instrument for medical optical tomography," *Rev. Sci. Instrum.* **71**, (1), 256–265 (2000).
26. J. Swartling, A. Bassi, C. D'Andrea, A. Pifferi, A. Torricelli, and R. Cubeddu, "Dynamic time-resolved diffuse spectroscopy based on supercontinuum light pulses," *Appl. Opt.* **44**, (22), 4684–4692 (2005).
27. L. Wang, P. P. Ho, C. Liu, G. Zhang, and R. R. Alfano, "Ballistic 2-D imaging through scattering walls using an ultrafast optical Kerr gate," *Science* **253**, 769–771 (1991).
28. C. D'Andrea, D. Comelli, A. Pifferi, A. Torricelli, G. Valentini, and R. Cubeddu, "Time-resolved optical imaging through turbid media using a fast data acquisition system based on a gated CCD camera," *J. Phys. D* **36**, 1676–1681 (2003).
29. G. M. Turner, G. Zacharakis, A. Soubret, J. Ripoll, and V. Ntziachristos, "Complete-angle projection diffuse optical tomography by use of early photons," *Opt. Lett.* **30**, (4), 409–411 (2005).
30. T. J. Brukilacchio, "A diffuse optical tomography system combined with x-ray mammography for improved breast cancer detection," Ph.D. Thesis, Department of Electrical Engineering, Tufts University, Boston, Mass. (2003).
31. A. Liebert, H. Wabnitz, D. Grosenick, and R. Macdonald, "Fiber dispersion in time domain measurements compromising the accuracy of determination of optical properties of strongly scattering media," *J. Biomed. Opt.* **8**, (3), 512–516 (2003).
32. M. S. Patterson, B. Chance, and B. C. Wilson, "Time-resolved reflectance and transmittance for the non-invasive measurement of tissue optical properties," *Appl. Opt.* **28**, (12), 2331–2336 (1989).
33. R. C. Haskell, L. O. Svaasand, T. T. Tsay, T. C. Feng, M. S. McAdams, and B. J. Tromberg, "Boundary conditions for the diffusion equation in radiative transfer," *J. Opt. Soc. Am. A* **11**, (10), 2727–2741 (1994).
34. F. Martelli, S. Del Bianco, and G. Zaccanti, "Procedure for retrieving the optical properties of a two-layered medium from time-resolved reflectance measurements," *Opt. Lett.* **28**, (14), 1236–1238 (2003).
35. C. Abrahamsson, T. Svensson, S. Svanberg, S. Andersson-Engels, J. Johansson, and S. Folestad, "Time and wavelength resolved spectroscopy of turbid media using light continuum generated in a crystal fiber," *Opt. Express* **12**(17), 4103–4112 (2004).
36. J. Swartling, J. S. Dam, S. Andersson-Engels, "Comparison of spatially and temporally resolved diffuse-reflectance measurement systems for determination of biomedical optical properties," *Appl. Opt.* **42**(22), 4612–4620 (2003).
37. R. Cubeddu, A. Pifferi, P. Taroni, A. Torricelli, and G. Valentini, "Experimental test of theoretical models for time-resolved reflectance," *Med. Phys.* **23**(9), 1625–1633 (1996).
38. V. Ntziachristos and B. Chance, "Accuracy limits in the determination of absolute optical properties using time-resolved NIR spectroscopy," *Med. Phys.* **28**(6), 1115–1124 (2001).
39. S. Fantini, M. A. Franceschini, and E. Gratton, "Semi-infinite-geometry boundary problem for light migration in highly scattering media: A frequency-domain study in the diffusion approximation," *J. Opt. Soc. Am. B* **11**, 2128–2138 (1994).